

Hydrodynamic Coefficients for Various Postures of the Underwater Manipulator

D. Duan[†], S. Ren, X. Zhang, Y. Cheng, X. Wang and H. Zhang

School of Mechanical Engineering, University of Jinan, Jinan, 250022, China

[†]Corresponding Author Email: me_duan@ujn.edu.cn

ABSTRACT

The hydrodynamic coefficients of underwater manipulators constantly change during their operation. In this study, the hydrodynamic coefficients of an underwater manipulator were calculated using the finite volume method to better explain its hydrodynamic performance. The drag, lift, and moment coefficients and the Strouhal number of an underwater manipulator for different postures were investigated. The results indicated that in each motion range, the coefficients first increase and then decrease. Meanwhile, when the attitude of the underwater manipulator is axis-symmetric or origin-symmetric, the hydrodynamic coefficients and the Strouhal number obtained are approximately the identical. The drag coefficient, lift coefficient and moment coefficient reach their maximum values of 3.59, 3.29, and 1.78 at angles of 30°, 150°, and 150°, respectively, with minimum values at 90°, 50° and -30°. Furthermore, the leading-edge shape of the underwater manipulator had a significant effect on the hydrodynamic coefficient. Maximum reductions of 44%, 25%, and 50.5% were obtained in the drag, lift, and moment coefficients, respectively, by comparing the semicircular leading edge with the right-angle leading edge. A maximum Strouhal number of 0.219 was obtained when the semicircular leading edge of the underwater manipulator was the upstream surface. This study will provide theoretical guidance to reveal the hydrodynamic performance of the underwater manipulators. It also serves as a reference for the structural design of the underwater manipulators.

Article History

Received June 10, 2023

Revised August 16, 2023

Accepted September 28, 2023

Available online December 4, 2023

Keywords:

Underwater manipulator

Drag coefficients

Lift coefficients

Moment coefficients

Strouhal number

Leading-edge shape

1. INTRODUCTION

With the continuous development of ocean exploration technologies, underwater manipulators are widely used for underwater collection, ocean exploration, and equipment maintenance (Fu et al., 2019). To create underwater manipulators with good working performance, it is necessary to build an accurate hydrodynamic model of underwater manipulators (Fan et al., 2012). However, unlike land-based manipulators, underwater manipulators must overcome its own weight and payload, as well as the effects of hydrodynamic forces and moments caused by the water environment (Kolodziejczyk, 2018). Therefore, it is important to investigate the hydrodynamic properties affecting underwater manipulators.

McLain & Rock (1998) discovered through underwater experiments that the water environment had a significant effect on the motion of an underwater

manipulator. Chae et al. (2020) observed through simulations that both the center of mass and reaction force change when the manipulator moves. Therefore, it was necessary to compensate for the effects of water flow. Wang et al. (2007) analyzed the dynamics of an underwater manipulator based on slicing theory and conducted simulation to demonstrate that the water flow deflects its motion trajectory. Xu et al. (2013) divided the hydrodynamics into two parts for analysis and calculation. The obtained hydrodynamic model was applied to the control system of an underwater manipulator with good results. The results of the above studies all indicated that water currents can have a significant effect on the motion of the underwater manipulator. In the above studies on hydrodynamics, the acquisition of hydrodynamic coefficients is crucial.

However, at present, the hydrodynamic coefficients cannot be directly derived from theory. Currently, the main methods for obtaining hydrodynamic coefficients

NOMENCLATURE			
B	underwater manipulator diameter	C_L	lift coefficient
L	underwater manipulator length	C_M	moment coefficient
V	water velocity	St	Strouhal number
α	rotation angle	f	vortex shedding frequency
C_D	drag coefficient	Ω	vorticity
ρ	fluid density	ν	dynamic viscosity coefficient
G_k	turbulent kinetic energy	δ_{ij}	Kronecker delta function
μ_t	turbulent viscosity	Re	Reynolds number
μ	hydrodynamic viscosity	G_ω	ω equation
Γ_k	effective diffusion terms of k	Y_k	divergence of k model
Γ_ω	effective diffusion terms of ω	Y_ω	divergence of ω model
D_ω	orthogonal divergence term	x_j	vertical directions
x_i	horizontal directions	t	time

are the model experiment and CFD numerical simulation methods (Safari et al., 2022). The model experimental method is less common because of its scale effects and required time and effort. Meanwhile, the CFD numerical simulation method is the mainstream method for hydrodynamic analysis of underwater manipulators because it has a short calculation period and no scale effect (Zhang et al., 2020). Both Racine & Paterson (2005) and Irwin & Chauvet (2007) verified the reliability of the CFD numerical simulation method by comparing the simulation results of the underwater manipulator with the engineering experiments. Zhao et al. (2009) concluded that the drag coefficient varied with the inclination angle of the cylinder by studying an infinitely long cylinder. Kolodziejczyk (2015, 2016) has calculated the joint moments of the underwater manipulator in eight different postures through CFD simulations. The results indicated that the joint moments in different postures were different. However, the drag and lift coefficients have not been studied. Zhang et al. (2019) concluded that the change in the motion posture of the underwater manipulator would lead to a change in the viscous hydrodynamic coefficient through numerical simulation.

In addition to the effects of posture, it is found that there are lateral and end-flow fields for the underwater manipulator as a combination of finite-length cylinders (Hölscher & Niemann, 1996; Cakir et al., 2015). However, most of the studies available on the cylindrical near-flow field have focused on the lateral flow. Chen et al. (2007) found that the drag coefficient obtained from the three-dimensional cylindrical model was smaller than that obtained from the two-dimensional model by studying the infinitely long cylindrical model. Cheng et al. (2022) investigated the effect of the cross-sectional shape of underwater manipulators on hydrodynamic coefficients. The results indicated that the smaller hydrodynamic coefficients were obtained when the cross-sectional shape was elliptical. Notably, Gao et al. (2018) found that the drag coefficient was significantly lower compared to the infinitely long model by the results of a study on a finite length cylinder with two free ends. Additionally, the law of environmental variations on the boundary layer has also been studied. He and Seddighi (2013) found that the transition from low Reynolds number turbulence to high Reynolds turbulence consists of three distinct phases. Mathur et al. (2018) observed that the transient flow is similar to the accelerated laminar

flow superimposed on the original constant flow base. Kharghani and PasandidehFard (2022) found a significant difference in the effect of time-accelerated flow on turbulence influenced by different pressure gradients. PasandidehFard and Naeimirad (2022) by further study found that higher momentum rate affects the thickness of the boundary layer and the forced flow rate changes the vortex shape. These studies show that the acceleration of the solid surface fluid has a significant effect on the force exerted on the fluid and that the change in the surface shape will lead to the acceleration of the surface fluid. Although all the above studies have investigated the hydrodynamics of the underwater manipulator, there was no systematic discussion on the law of the influence of the posture on the hydrodynamic coefficients in the dynamic water environment. Therefore, we need to study this to supplement and improve the current research status.

Based on the aforementioned studies, the posture of the underwater manipulator and the axial flow of the fluid at the end face both affect the hydrodynamic performance. Since it is not possible to study the end-surface winding flow influence law independently in three dimensions, the present paper will carry out numerical simulations on the two-dimensional model of an underwater manipulator to investigate the influence of the underwater manipulator posture on the hydrodynamic coefficients in the end-surface winding flow. In this study, the drag, lift, and moment coefficients, as well as the Strouhal number, were calculated for different postures of the underwater manipulator. The effect of the leading-edge shape of the underwater manipulator on the hydrodynamic coefficients and Strouhal number was also discussed. This study contributes to a more accurate hydrodynamic model of underwater manipulators, which can improve the performance of underwater manipulators, such as sea cucumber fishing robots, through feedforward control. Meanwhile, this study also serves as a theoretical guide role for the structural design of underwater manipulators.

The paper is organized as follows. The model building, including the model introduction, boundary conditions, mesh discretization, mesh independence, and numerical validation, is presented in Section 2. Subsequently, Section 3 discusses the laws of influence of the posture of the underwater manipulator arms in terms of the drag, lift, and moment coefficients and

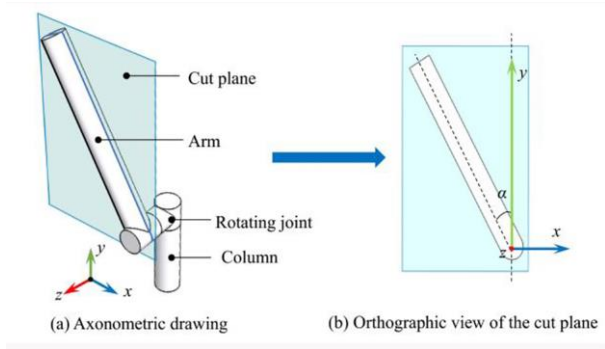


Fig. 1 Schematic diagram of the underwater manipulator

Strouhal number. Finally, conclusions are summarized in Section 4.

2. MODEL BUILDING

2.1 Model and Boundary Condition Setting

Figure 1(a) shows a model of a single-degree-of-freedom underwater manipulator. In Fig. 1(b), α is the angle between the axis of the underwater manipulator and y -axis. Figure 1(b) shows the cut plane in the middle of the underwater manipulator, which was obtained using the cutting method shown in Fig. 1(a). The upper end of the obtained 2D underwater manipulator was right-angle in shape, whereas the lower end was semicircular. Based on this, a two-dimensional fluid computing domain model was established for the subsequent simulation.

Figure 2 illustrates the boundary conditions for calculating hydrodynamic coefficients. The semicircle diameter is $B=30$ mm, and the total length of the model is $L=10B$. The left side of the fluid domain was the velocity inlet of the fluid and the right side was the pressure outlet. The no slip boundary condition was applied to walls on both sides. The distance between the model and inlet of the flow field was $5L$, and the distance from the outlet was $20L$. The distance between the upper and lower boundaries of the calculation domain was $16L$. V represents the constant current along the positive direction of the x -axis.

Figure 3 shows the angles of the model and the positions of the coordinate axes of the computational domain. In this study, the vertical posture was defined as $\alpha=0^\circ$ when the angle α between the model and flow direction was 90° . The rotation to the right and left was positive and negative, respectively; thus, the range of α was $-180^\circ \leq \alpha \leq 180^\circ$. Although the range of rotation of the underwater manipulator is not -180° to 180° in reality, the range is accessible for analysis and is more conducive to the completeness of the results of the study. The coordinate origin of the calculation domain was located at the center of the circle at the end of the model. While as the angle α keeps varying, the height of the manipulator model in the vertical flow field direction and the width correlation in the parallel flow field direction keep changing along with it. Since the drag coefficient and lift coefficient are affected by their height and width, the

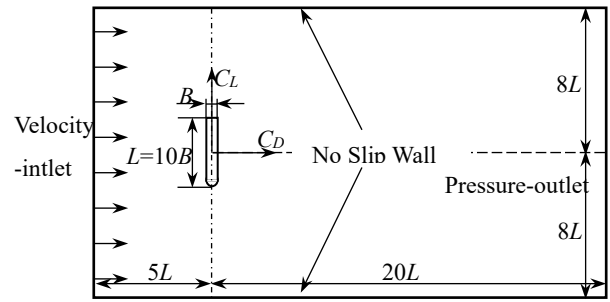


Fig. 2 Schematic diagram of computational domain model

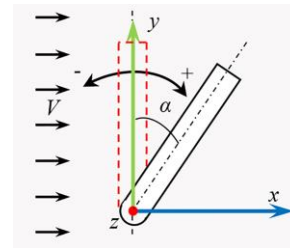


Fig. 3 Diagram of coordinate axes and angles

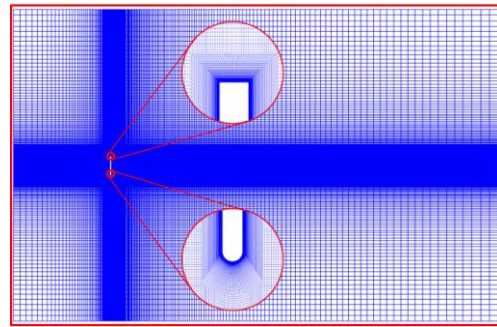


Fig. 4 Meshing scheme

relationship between the angle α and hydrodynamic coefficient is also further discussed in this paper.

2.2. Meshing

To determine a suitable meshing method, a structured mesh was used to divide the computational domain. As an example, a model with angle $\alpha=0^\circ$ (vertical posture) was divided into three meshes with different numbers of boundary layers for the calculation. The grid size of the first wall layer is 0.01 mm. The grid results are shown in Fig. 4. The simulation results for different grid conditions are listed in Table 1.

In this work, the results obtained under different meshes were compared by continuously refining the encryption, judging the convergence of the solutions of different meshes, and obtaining the simulation results that meet the requirements of high accuracy.

As shown in Table 1, the calculated drag coefficients C_D and Strouhal number St did not significantly change with an increased number of grids. The maximum error in C_D was 4.0%, and there was no change in St . Therefore,

Table 1 Grid independence verification

Group	Elements	C_D	Relative error	St	Relative error
1	98232	2.74	—	0.051	—
2	109472	2.65	3.28%	0.051	0
3	127692	2.63	4.0%	0.051	0

Table 2 Accuracy verification of turbulence model $k-\omega$ SST

Re	C_D	Relative error	St	Relative error	Data source
21000	1.99	—	0.129	1.4%	Present result
21000	—	—	0.131	—	Chen & Liu (1999)
21400	1.99	3.4%	0.134	1.5%	Present result
21400	2.06	—	0.132	—	Lyn et al. (1995)
68000	2.07	2.6%	0.132	4.4%	Present result
68000	2.12	—	0.138	—	Wang et al. (2021)
200000	2.09	0.4%	0.132	6.4%	Present result
200000	2.08	—	0.124	—	Bi et al. (2012)

to ensure the accuracy of the calculation results and save computing resources simultaneously, the division method of the first group of grids was adopted.

2.3. Verification of the Numerical Method

The two-dimensional incompressible flow around the underwater manipulator is represented by the Navier–Stokes dimensionless equation. Assuming that neither the density nor the viscosity of the fluid in the flow field changes. (Qu et al., 2021) The expressions in the rectangular coordinate system are as follows:

$$\frac{\partial U_i}{\partial x_i} = 0 \quad (3)$$

$$\frac{\partial U_i}{\partial t} + U_j \frac{\partial U_i}{\partial x_j} = -\frac{1}{\rho} \frac{\partial P}{\partial x_i} + \nu \frac{\partial^2 U_i}{\partial x_j^2} - \frac{\partial \overline{u_i u_j}}{\partial x_j} \quad (4)$$

Where, x_i and x_j represent the horizontal and vertical directions, respectively. U_i and U_j are the corresponding mean velocity components $\overline{u_i u_j}$ is the Reynolds stress component. ρ is the fluid density. P is the dynamic pressure. ν represents the dynamic viscosity coefficient. The Reynolds stress component $\overline{u_i u_j}$ is expressed in terms of turbulent viscosity and the mean flow gradient using the Boussinesq approximation is

$$-\overline{u_i u_j} = \mu_t \left(\frac{\partial U_i}{\partial x_j} + \frac{\partial U_j}{\partial x_i} \right) - \frac{2}{3} \delta_{ij} G_k \quad (5)$$

Where G_k represents turbulent kinetic energy, μ_t is the turbulent viscosity, and δ_{ij} is the Kronecker delta function. The equations are non-dimensionalized with appropriate length and velocity scales.

$$\frac{\partial U_i}{\partial t} + U_j \frac{\partial U_i}{\partial x_j} = -\frac{\partial P}{\partial x_i} + \frac{1}{Re} \frac{\partial^2 U_i}{\partial x_j^2} - \frac{\partial \overline{u_i u_j}}{\partial x_j} \quad (6)$$

Re corresponds to the Reynolds number. It is the dimensionless parameters used to describe the fluid flow state.

$$Re = \frac{\rho U D}{\mu} \quad (7)$$

Where μ is the hydrodynamic viscosity. D is the hydraulic diameter of the section

A suitable turbulence model is key to obtaining accurate calculation results. Because the model in this study was similar to a square, the $k-\omega$ SST turbulence model, which is widely used in the simulation calculations of the flow around a square cylinder, was selected. This turbulence model combines the advantages of the $k-\omega$ and $k-\varepsilon$ models. The original $k-\omega$ model was used near the wall, whereas the $k-\varepsilon$ model was used in the far field. The results obtained using the $k-\omega$ SST turbulence model simulate the surrounding flow more accurately (Wan et al., 2010). The governing equations of the turbulence model are k equation and ω equation. The equation consists of two parts, and the expressions are as follows:

$$\frac{\partial(\rho k)}{\partial t} + \frac{\partial(\rho k U_i)}{\partial x_i} = \frac{\partial(\Gamma_k \frac{\partial k}{\partial x_j})}{\partial x_j} + G_k - Y_k + S_k \quad (8)$$

$$\frac{\partial(\rho \omega)}{\partial t} + \frac{\partial(\rho \omega U_i)}{\partial x_i} = \frac{\partial(\Gamma_\omega \frac{\partial \omega}{\partial x_j})}{\partial x_j} + G_\omega - Y_\omega + D_\omega + S_\omega \quad (9)$$

In the equation, G_ω by ω equation. Γ_k and Γ_ω represent the effective diffusion terms of k and ω respectively. Y_k and Y_ω represent the divergence of k and ω respectively. D_ω represents the orthogonal divergence term. S_k and S_ω are user defined.

The hydraulic diameter of the two-dimensional model of the underwater manipulator arm varies with the posture, which will lead to a change in the Reynolds number. Therefore, the Reynolds number range corresponding to the model in this paper can be obtained through equation (7) is $1.5 \times 10^4 \leq Re \leq 1.5 \times 10^5$. So, the accuracy verification of the turbulence model must also be within this range.

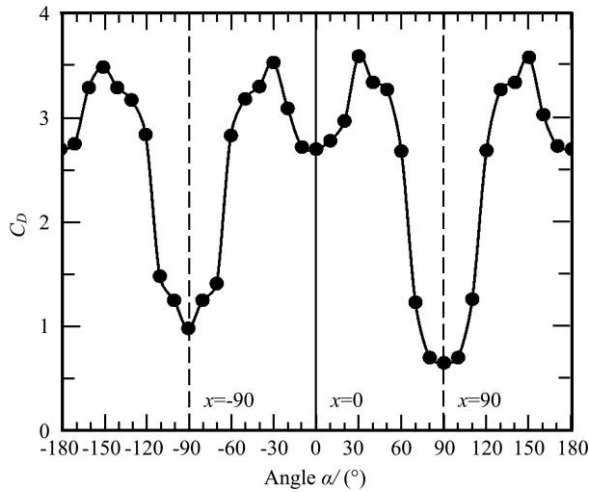


Fig. 5 Relationship between the drag coefficients C_D and the angles

To verify the reliability of the turbulence model, the $k-\omega$ SST turbulence model was used under different Re values, and the results were compared with those reported in the literature. The calculation results are listed in Table 2. The data in Table 2 indicate that C_D and St calculated using this turbulence model are in good agreement with those in existing literature. The maximum errors of the C_D and St were 3.4% and 6.4%, respectively. Therefore, we believe that the turbulence model $k-\omega$ SST can be used appropriately in the present study.

3. RESULTS AND DISCUSSION

3.1 Drag Coefficient

Figure 5 shows C_D of the underwater manipulator for different postures. From Fig. 5, C_D were divided into four motion ranges in the range $-180^\circ \leq \alpha \leq 180^\circ$; the trend of change in each range increased and then decreased. When $-90^\circ \leq \alpha \leq 0^\circ$, the change of C_D can be further divided into three stages. As the α increased from -90° to -60° , the increase in the C_D was higher and its value increased by a factor of 2.88. When the α increased from -60° to -30° , the growth rate of the C_D slowed down significantly, and reached the maximum value of 3.53 at -30° , increasing by 1.25 times. Finally, there was a decreasing trend in the range of $-30^\circ \leq \alpha \leq 0^\circ$, reaching a minimum value of 2.14 at 0° . In the range of $90^\circ \leq \alpha \leq 180^\circ$, the C_D presented the same pattern of change. Nevertheless, for $0^\circ \leq \alpha \leq 90^\circ$, the change in C_D can be divided into two stages. First, for $0^\circ \leq \alpha \leq 30^\circ$, C_D increased by 33% and reached a maximum value of 3.59 at $\alpha=30^\circ$. Second, for $30^\circ \leq \alpha \leq 90^\circ$, C_D significantly decreased by 81.9% and reached a minimum value of 0.65 at $\alpha=90^\circ$.

The maximum value of C_D was approximately 5.52 times than the minimum value. In the $-180^\circ \leq \alpha \leq -90^\circ$, C_D exhibit the same law of variation. As shown in Fig. 6, the trend of C_D was consistent with that reported by [Norberg \(1993\)](#). However, the variation in the curve of C_D in this

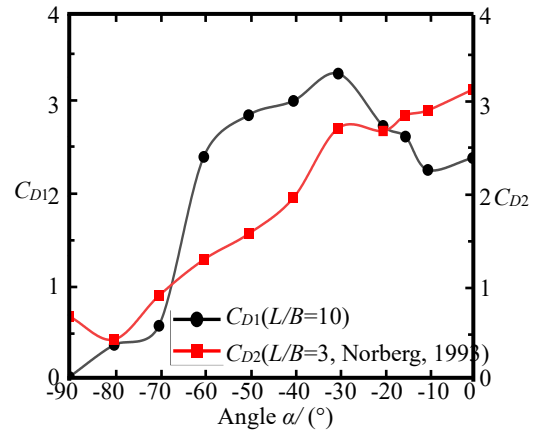


Fig. 6 Relationship between the drag coefficients C_D and the angles under different L/B

study was more pronounced. This was because larger section length to width ratio (L/B) of the model was used in this study, which precisely validated the law that the postures affect C_D more significantly for larger L/B .

From Fig. 5, C_D were all positive at different values of α . This indicates that the drag direction was always the same as the incoming flow direction, that is, horizontally to the right. C_D were symmetrically distributed on the left and right with respect to the line $x=0$ in the range $-180^\circ \leq \alpha \leq 180^\circ$. This means that the values of the C_D for the two poses symmetric along the y -axis are very close to each other. From the numerical relation of α , the values of the C_D were closer when the angles are opposite. For example, $C_D = 3.59$ when $\alpha = 30^\circ$ and $C_D = 3.53$ when $\alpha = -30^\circ$, which can be seen to be very close. In addition, C_D was approximately locally symmetric on the left and right sides of the line $x=0$. For $-180^\circ \leq \alpha \leq 0^\circ$, C_D was approximately symmetrical with respect to the line $x=-90$. For $0^\circ \leq \alpha \leq 180^\circ$, C_D was nearly symmetrically distributed with respect to the line $x=90$. This implies that C_D of the two postures are approximately symmetric with respect to the x -axis. From the numerical relation of α , C_D was the same when the sum of α was -180° or 180° , such as the values of 3.53 and 3.5 for $\alpha=-30^\circ$ and -150° , respectively, the values of C_D were very close to each other.

Figure 7 shows the velocity contours of the flow field for the underwater manipulator at angles -150° , -30° , 30° , and 150° . From the velocity contours, these four postures were in the same flow field environment; thus, the force of the flow field on the underwater manipulator was the same. Figure 8 illustrates the variation curves of C_D for these four postures. These symmetrical postures had the same C_D because of identical C_D variation curves for the same period.

However, when the angle was $\pm 80^\circ$, $\pm 90^\circ$, and $\pm 100^\circ$, C_D did not conform to the aforementioned law. Figure 5 shows that C_D for angles of -80° , -90° , and -100° were significantly larger than those for angles of 80° , 90° , and 100° . These differences were 44%, 33.7%, and 44%,

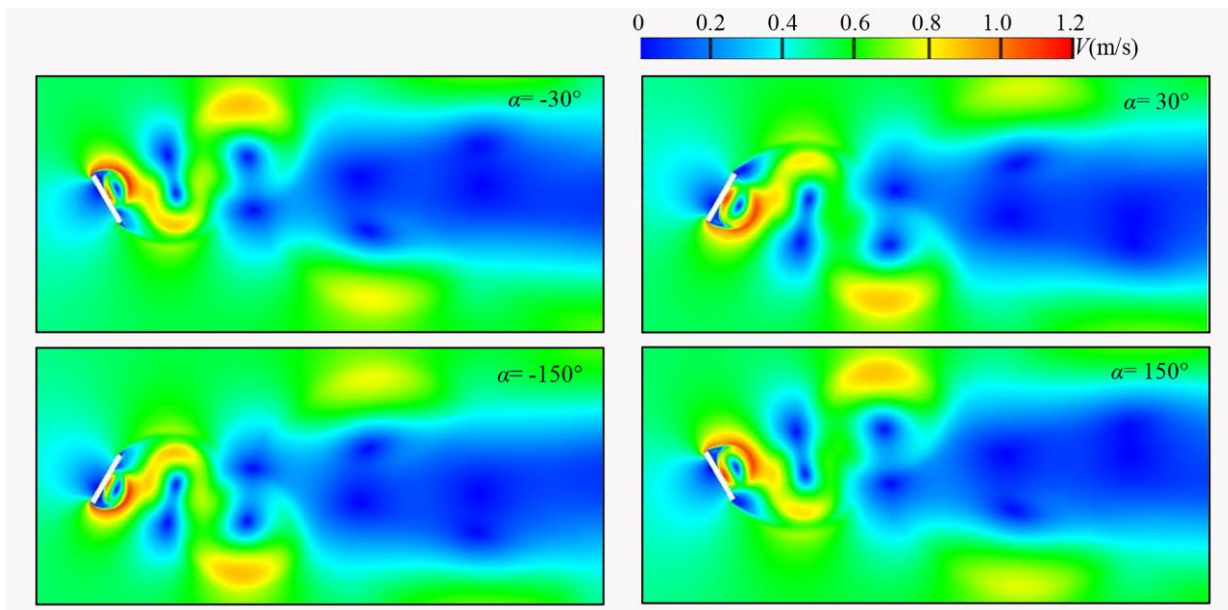


Fig. 7 Velocity contours at the same moment under the angle α of -150° , -30° , 30° and 150°

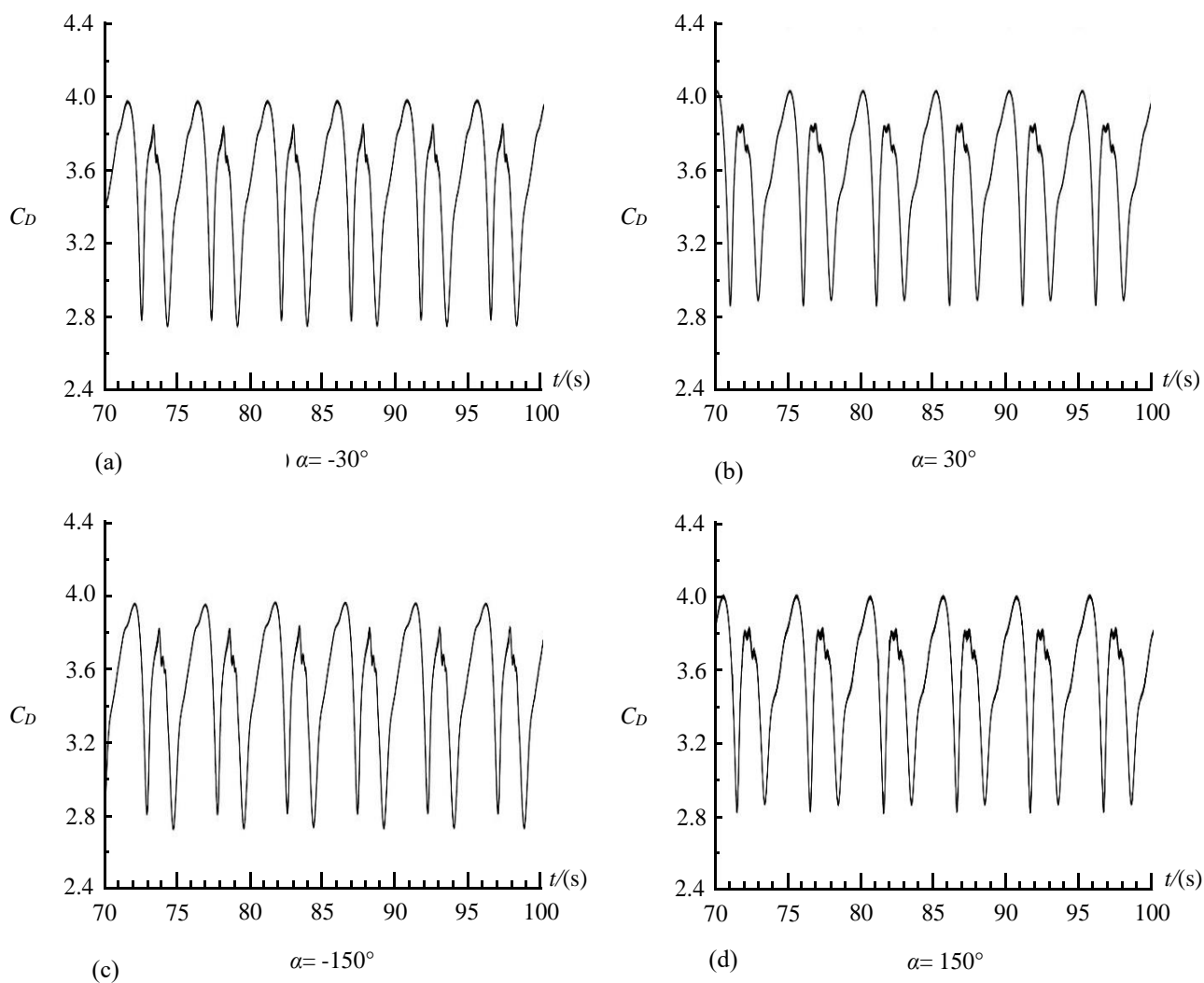


Fig. 8 Drag coefficient curves when the angles were -150° , -30° , 30° and 150°

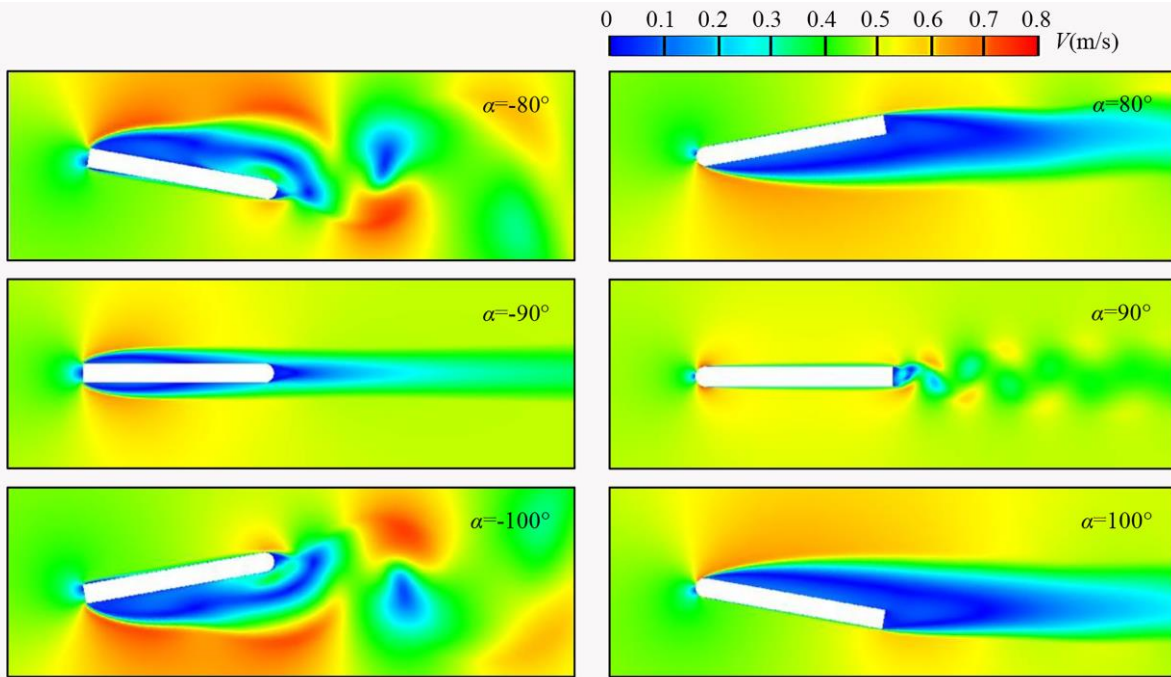


Fig. 9 Velocity contours at the same moment under the angle α of -100° , -90° , -80° , 80° , 90° and 100°

respectively. This was because the shape of the leading edge had a more significant effect on C_D at these angles. From Fig. 9, the leading edge of the underwater manipulator was right-angle in shape and semicircular at positive and negative angles of 80° , 90° , and 100° , respectively. Figure 9 shows that although the postures of the underwater manipulator were symmetric, the flow field in the vicinity of the underwater manipulator was significantly different because of the difference in the shape of the leading edge. This also led to a difference in C_D of the underwater manipulator in these postures. A comparison of the data in Fig. 5 shows that C_D of the underwater manipulator with a semicircular leading edge are lower than those of the right-angle leading edge. This conclusion was confirmed by Du et al. (2017). Thus, when the shape of the leading edge is the same, the underwater manipulator with a symmetrical posture has the same C_D that is applicable for all postures.

3.2 Lift Coefficient

Figure 10 shows C_L for different postures of the underwater manipulator. From Fig. 10, C_L were also divided into four motion ranges in the range $-180^\circ \leq \alpha \leq 180^\circ$; the trend of each range first increased and then decreased. C_L varied in the range of -3.29 to 3.29 as the posture of the underwater manipulator changed. A positive value indicated that the direction of the lift was vertically upward, and a negative value indicated that it was vertically downward. Thus, the lift was vertically downward in the ranges $-180^\circ \leq \alpha \leq -90^\circ$ and $0^\circ \leq \alpha \leq 90^\circ$ and upward in the ranges $-90^\circ \leq \alpha \leq 0^\circ$ and $90^\circ \leq \alpha \leq 180^\circ$.

For $0^\circ \leq \alpha \leq 180^\circ$, the change in C_L can be divided into four stages. First, for $0^\circ \leq \alpha \leq 30^\circ$, C_L gradually increased and reached an extreme value of -3.29 at $\alpha = 30^\circ$. Second, for $30^\circ \leq \alpha \leq 90^\circ$, C_L gradually decreased and reached a minimum value of 0 at $\alpha = 90^\circ$. Third, for $90^\circ \leq \alpha \leq 150^\circ$, C_L

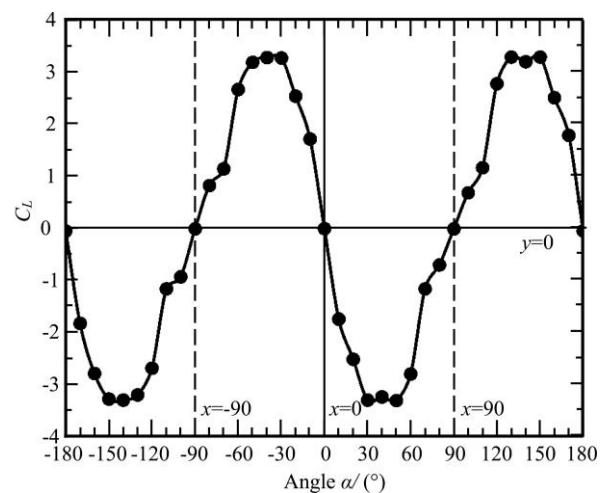


Fig. 10 Relationship between C_L and α

became positive, which means that the direction of the lift began to change vertically upward. Then, C_L gradually increased and reached a maximum value of 3.29 at $\alpha = 150^\circ$. Fourth, for $150^\circ \leq \alpha \leq 180^\circ$, C_L decreased gradually and returned to the same state as when $\alpha = 0^\circ$. A similar trend of the change in C_L was observed for $-180^\circ \leq \alpha \leq 0^\circ$. The trend of C_L was consistent with that reported by Norberg (1993), as shown in Fig. 11. Both exhibited a rising and then decreasing trend in variation. However, the variation curves in their study were smoother because the aspect ratio of the model was smaller ($L/B=3$) compared to that in this study ($L/B=10$). Therefore, the change in C_L was more visible in this study.

From Fig. 10, C_L were almost symmetrically distributed about the origin $(0,0)$ point in the range $-180^\circ \leq \alpha \leq 180^\circ$. In particular, C_L values of the two postures

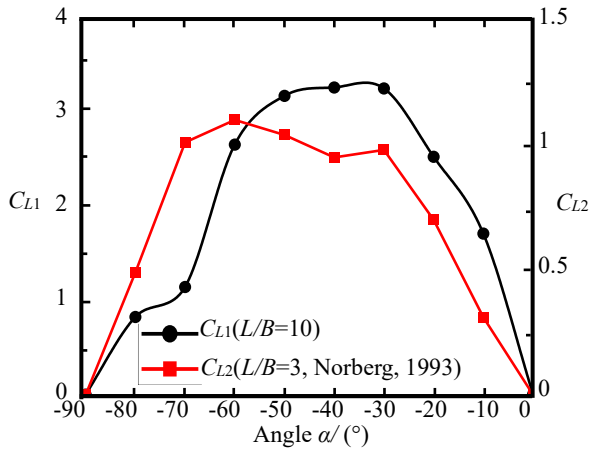


Fig. 11 Relationship between C_L and α under different L/B

with respect to the y-axis symmetry were nearly equal, but in the opposite direction. From the numerical relationship of α , when the two angles representing the posture were opposite to each other, C_L of the models were similar in magnitude and opposite in direction. For example, when $\alpha = -30^\circ$, the value of C_L was 3.27 and $C_L = -3.28$ in the case of $\alpha = 30^\circ$. In addition, C_L exhibited a local symmetrical distribution on both sides of the line $x=0$. For

$-180^\circ \leq \alpha \leq 0^\circ$, C_L was symmetrically distributed with respect to point $(-90,0)$. For $0^\circ \leq \alpha \leq 180^\circ$, C_L was symmetrically distributed with respect to point $(90,0)$. This implies that C_L approximately the same magnitude and in opposite directions for the two postures with respect to the x-axis symmetry. From the numerical relationship of α , when the sum of the two angles was equal to -180° or 180° , C_L in these two postures were similar in magnitude and opposite in direction. For example, for angles of -30° and -150° , the values of C_L were 3.27 and -3.26, respectively.

Figure 12 shows the curves of C_L variation for the same period at angles -150° , -30° , 30° , and 150° . The postures corresponding to these four angles were symmetric along the coordinate axis or the origin. The mean C_L values were the same for these four postures because their C_L variation curves were identical in magnitude and period. The only difference was the lift direction, which was represented as either positive or negative.

Figure 10 shows that there was also a significant difference in C_L when α was -80° versus 80° and -100° versus 100° . They differ by 16.9% and 25%, respectively, indicating that the leading-edge shape also affects C_L . In terms of the magnitude of the data, C_L of the underwater manipulator with semicircular leading edges were smaller than those with right-angled leading edges for the same or symmetrical posture. This conclusion was confirmed by Ajith et al. (2015).

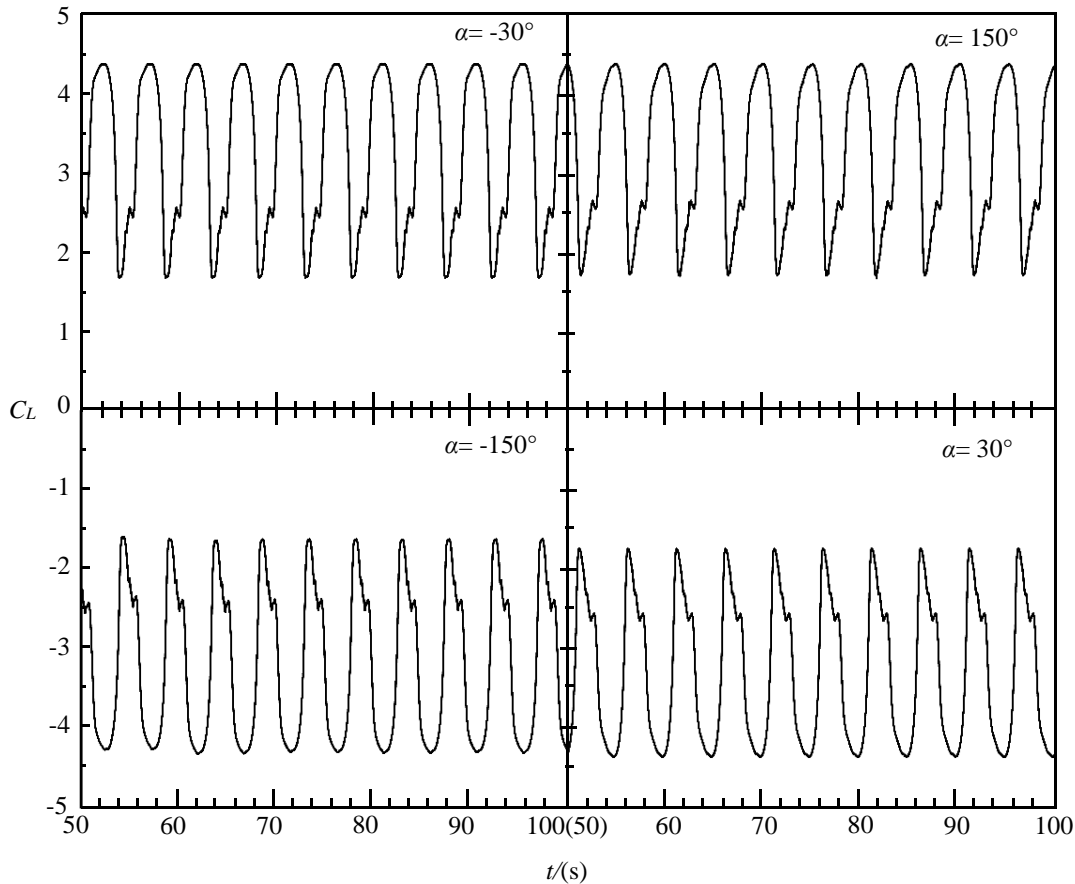


Fig. 12 Lift coefficient curves when the angle was -150° , -30° , 30° and 150°

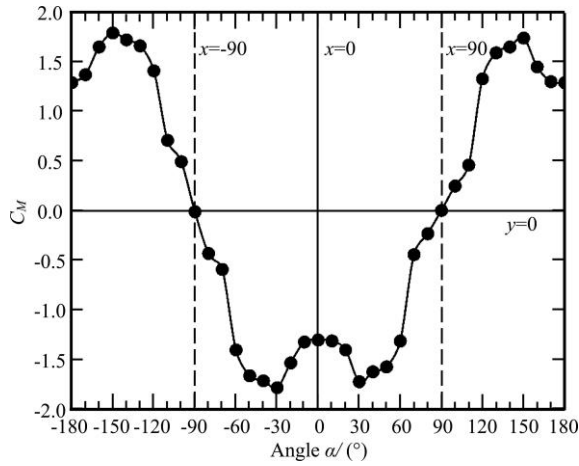


Fig. 13 Relationship between the moment coefficient C_M and angle α

3.3 Moment Coefficient

In this section, the moment coefficients of the underwater manipulator arm for different postures were discussed. The moment coefficients were defined as

$$C_M = \frac{M}{\frac{1}{2} \rho V^2 A_M} \quad (10)$$

Where M is the hydrodynamic moment applied to the underwater manipulator, A_M is the area impacted by the flow of water, V is the velocity of the water flow.

Figure 13 illustrates the moment coefficients C_M of the underwater manipulator for different postures. From Fig. 13, C_M were similarly divided into four motion ranges in the range $-180^\circ \leq \alpha \leq 180^\circ$; the trend in each range first increased and then decreased. C_M varied in the range of -1.78 to 1.78 as the posture changed.

Positive and negative values represent only the direction of the moment and do not affect the value. In this study, the positive and negative values represent counterclockwise and clockwise directions, respectively. Therefore, from Fig. 13, for $-90^\circ \leq \alpha \leq 90^\circ$, the moment on the model was in the clockwise direction. For $-180^\circ \leq \alpha \leq -90^\circ$ and $90^\circ \leq \alpha \leq 180^\circ$, the moment on the model was in the counterclockwise direction.

From Fig. 13, it can be seen that at $0^\circ \leq \alpha \leq 180^\circ$, the C_M variation is mainly divided into four stages. First, for $0^\circ \leq \alpha \leq 30^\circ$, the C_M gradually increased along the clockwise direction, and reached the maximum at $\alpha = 30^\circ$, with a value of 1.78. Second, when $30^\circ \leq \alpha \leq 90^\circ$, the C_M gradually decreased along the clockwise direction, and reached a minimum value of 0 when $\alpha = 90^\circ$. Third, for $90^\circ \leq \alpha \leq 150^\circ$, C_M became positive, which means that the direction of the moment changed from clockwise to counterclockwise. Then, C_M gradually increased and reached a maximum value of 1.78 in the counterclockwise direction at $\alpha = 150^\circ$. Fourth, for $150^\circ \leq \alpha \leq 180^\circ$, C_M decreased gradually and returned to the same state as when $\alpha = 0^\circ$. A similar trend of the change in C_M was observed for $-180^\circ \leq \alpha \leq 0^\circ$. In addition, the trend of the variation in the range $0^\circ \leq \alpha \leq 90^\circ$

was consistent with that of C_M curves obtained in the study by Sollic and Danbon (1999).

From Fig. 13, C_M were symmetrically distributed relative to the line $x=0$ in the range $-180^\circ \leq \alpha \leq 180^\circ$. This implies that when the two postures are symmetric along the y -axis, the underwater manipulators have the same C_M magnitude and direction. From the value of α , C_M were the same when the angles of the two postures were opposite to each other, such as -30° and 30° . Local symmetry was also observed in the C_M on the left and right sides. For $-180^\circ \leq \alpha \leq 0^\circ$, C_M were symmetrically distributed at the point $(-90, 0)$. For $0^\circ \leq \alpha \leq 180^\circ$, C_M were symmetrically distributed at the point $(90, 0)$. This implies that when the two postures were symmetric along the x -axis, their C_M were equal in magnitude and opposite in direction. In terms of the value of α , when the sum of the two α was equal to -180° or 180° , C_M of the link models in these two postures were equal in magnitude and opposite in direction, such as -150° and -30° and 30° and 150° .

From Fig. 13, when α was -80° versus 80° and -100° versus 100° , C_M did not follow the aforementioned rules. They differ by 45.3% and 50.5%, respectively. It was caused by the difference in the leading-edge shape of the models, which led to different changing patterns of the near-flow fields. In terms of the magnitude of the data, C_M of the underwater manipulator with semicircular leading edges were smaller than those with right-angled leading edges for the same or symmetrical posture.

3.4 Strouhal Number

In this section, the similarity criterion Strouhal number St was introduced when discussing physical similarity, which were defined as,

$$St = \frac{fD}{V} \quad (11)$$

Where, f is the vortex shedding frequency, D is the hydraulic diameter of the model.

Figure 14 shows St at different angles. From Fig. 14, the trend of St on both sides of the line $x=0$ was the same, except for a few special points. The variation trend of St was roughly divided into six stages within the range $0^\circ \leq \alpha \leq 180^\circ$. First, for $0^\circ \leq \alpha \leq 50^\circ$, St increased monotonically. Second, for $50^\circ \leq \alpha \leq 70^\circ$, St gradually decreased. Third, for $70^\circ \leq \alpha \leq 90^\circ$, St increased rapidly and reached an extreme value of 0.219 at $\alpha = 90^\circ$. Fourth, for $90^\circ \leq \alpha \leq 110^\circ$, St rapidly decreased. Fifth, for $110^\circ \leq \alpha \leq 130^\circ$, St gradually increased. Sixth, for $130^\circ \leq \alpha \leq 180^\circ$, St decreased monotonically and returned to the same state as when $\alpha = 0^\circ$ at $\alpha = 180^\circ$. A similar trend of the variation in St was observed for $-180^\circ \leq \alpha \leq 0^\circ$. The only difference is that at an angle of 90° , $St = 0.219$, whereas the $St = 0$ for an angle of -90° . This is due to the fact that due to the shape of the leading edge of the model, the separated shear layer did not reattach to the upper and lower surfaces of the model, and the rear vortex of the model was not shed.

From Fig. 14, St was symmetrically distributed along the line $x=0$ in the range $-180^\circ \leq \alpha \leq 180^\circ$, except for a few special points. This implies that f was equal when the two postures were symmetric along the y -axis, such as the

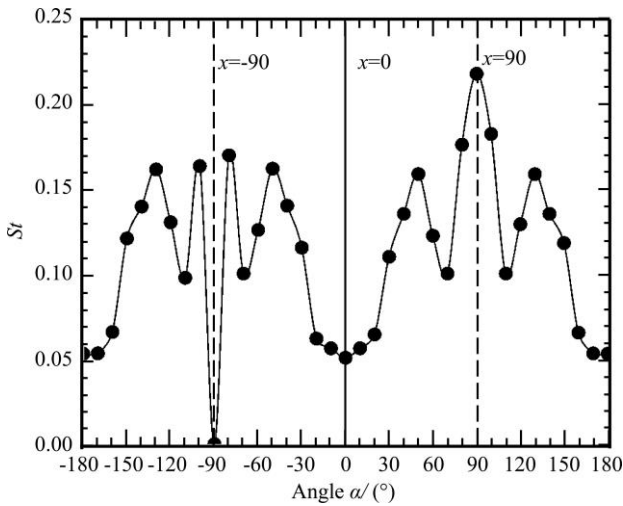


Fig. 14 Strouhal number St for each posture

postures represented by the angles -30° and 30° . For $-180^\circ \leq \alpha \leq 0^\circ$ and $0^\circ \leq \alpha \leq 180^\circ$, St also satisfied the locally symmetrical distribution. When the two postures were symmetric along the x -axis or the sum of the absolute values of α was equal to 180° , f after the flow field flows around the model was equal, such as -110° and -70° and 70° and 110° . In summary, except for a few postures that are significantly affected by the leading-edge shape, when the postures were symmetric along the coordinate axis or origin, the fluid have the same f after bypassing the flow. Figure 15 showed the vorticity contours of the flow field near each posture at the same moment with angles -110° , -70° , 70° , and 110° . The underwater manipulators of these postures had the same St because the water flowing through them produced the same vortex at the wake.

The aforementioned variation law applied to most angles with the exception of a few angles that were more significantly affected by the leading-edge shape. As shown in Fig. 15, these angles were -100° , -90° , -80° , 80° , 90° , and 100° . The difference between -90° and 90° was

particularly clear. St had maximum and minimum values of 0.219 and 0 at 90° and -90° , respectively. This difference was caused by the different shapes of the leading edges of the underwater manipulators. As shown in Fig. 16, the rear vortex of the model was not shed at $\alpha = -90^\circ$ because the separated shear layer did not reattach to the upper and lower surfaces of the model. At $\alpha = 90^\circ$, the leading edge of the model was shaped as a semicircle, and it reduced the size of the separation bubble formed when the fluid was separated. This makes it easier for the fluid to reattach to the model after being separated by the leading edge, thus allowing vortex shedding to form at the trailing end. Therefore, the fluid shear layer is more likely to hit and adhere to the upper and lower surfaces of the model after passing through the semicircular leading edge and form alternating shedding vortices. In terms of the numerical magnitude, the semicircular leading edge can lead to a larger St and f . In addition, when the semicircular leading edge of the underwater manipulator was the upstream surface, a maximum St of 0.219 was obtained.

To summarize the above, both hydrodynamic coefficients (C_D , C_L , and C_M) and St were divided into four motion intervals in the range of $-180^\circ \leq \alpha \leq 180^\circ$. C_D , C_L , and C_M increased, and then decreased in each range, whereas the variation in St in each range was a bit more complicated. The magnitude of hydrodynamic coefficients and St were nearly the same when the underwater manipulators postures were symmetric about the coordinate axis or the coordinate origin. The direction of C_D is always the same as the direction of the current, whereas the direction of C_L and C_M are related to the motion interval where the underwater manipulator is located. In addition, the shape of the leading edge of the underwater manipulator has significant effects on the hydrodynamic coefficients and St at angles of $\pm 80^\circ$, $\pm 90^\circ$, and $\pm 100^\circ$. Compared to the right-angle leading edge, the semicircular leading edge decreases the hydrodynamic coefficients, but increases St .

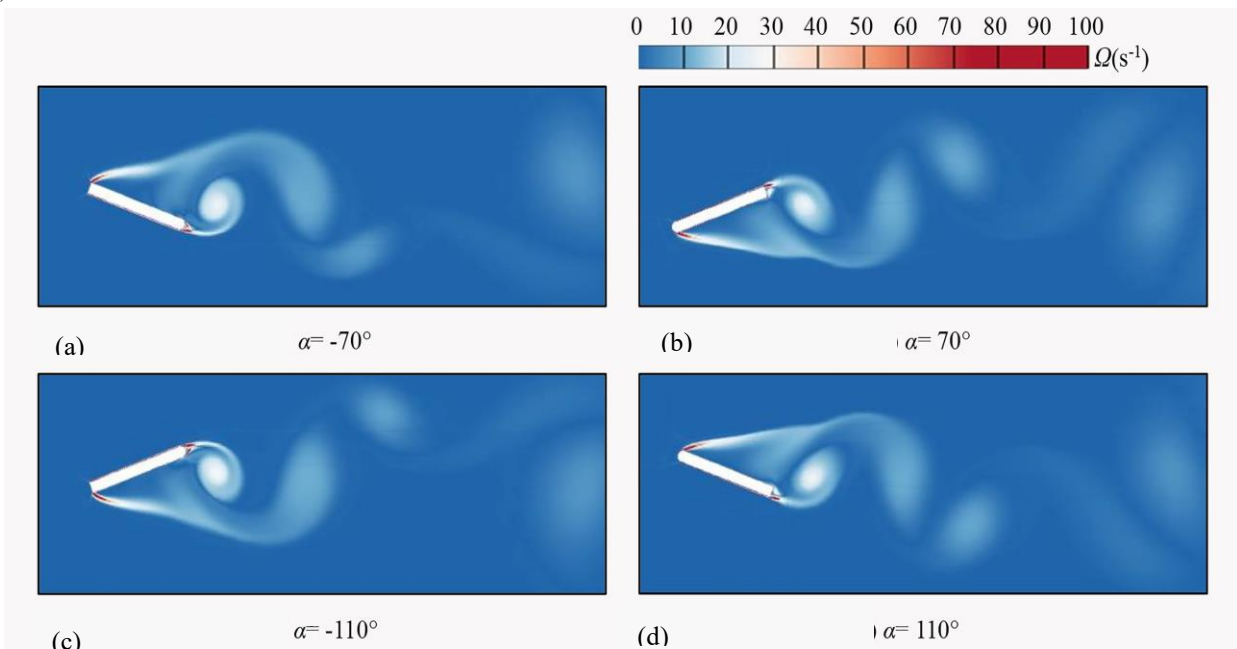


Fig. 15 Vorticity contours at the same moment under the angle α of -110° , -70° , 70° and 110°

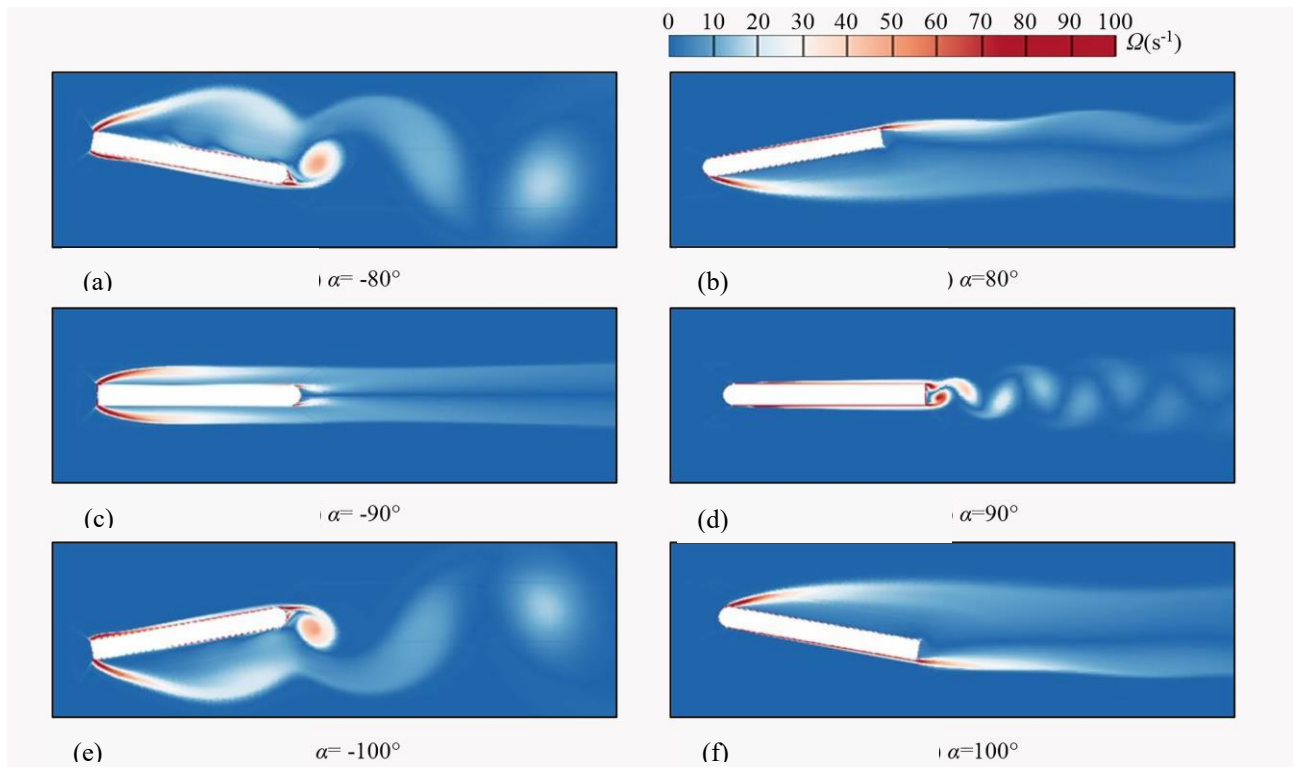


Fig. 16 Vorticity contours at the same moment under the angle α of -100° , -90° , -80° , 80° , 90° and 100°

4. CONCLUSION

The hydrodynamic coefficients (C_D , C_L , and C_M) and St of the underwater manipulator under different postures in a constant current environment were obtained through simulation. The data analysis revealed that the manipulator posture had a significant effect on these parameters and the major conclusions are as follows.

(1) The trends of C_D , C_L , and C_M in the range $-180^\circ \leq \alpha \leq 180^\circ$ can be divided into four motion ranges. The hydrodynamic coefficients in each motion range first increased and then decreased.

(2) Almost the same hydrodynamic coefficients and Strouhal numbers were obtained when the posture of the underwater manipulator was axis- or origin-symmetric. With the change in posture, C_D , C_L , and C_M varied in the range 0.65 to 3.59, -3.29 to 3.29, and -1.78 to 1.78, respectively.

(3) The shape of the leading edge of the underwater manipulator had a significant effect on the hydrodynamic coefficients. Maximum reductions of 44%, 25%, and 50.5% were obtained in C_D , C_L , and C_M , respectively, by comparing the semicircular leading edge with the right-angle leading edge.

(4) The shape of the leading edge of the underwater manipulator also affected St . The semicircular leading edge resulted in a larger St than the right-angle leading edge. In addition, a maximum St of 0.219 was obtained when the semicircular leading edge was the upstream surface ($\alpha = 90^\circ$).

The study findings intuitively expound the relationship between the postures of the manipulator and hydrodynamic coefficients. This helps to develop a high-precision hydrodynamic model of the underwater manipulator, which can improve the working performance of the underwater manipulator through feedforward control. In addition, this study can also provide theoretical guidance for the structural design of underwater manipulators, such as the use of circular appearance can decrease hydrodynamic interference.

ACKNOWLEDGEMENTS

This project is supported by National Natural Science Foundation of China (No.51905211) and A Project of the “20 Regulations for New Universities” funding program of Jinan (No.202228116).

CONFLICT OF INTEREST

We declare that we do not have any commercial or associative interest that represents a conflict of interest in connection with our work submitted.

AUTHORS CONTRIBUTION

Derong Duan: Methodology, Validation, Investigation, Writing – original draft. **Shanbin Ren:** Conceptualization, Formal analysis, Writing-Revision. **Xiaoya Zhang:** Review, editing. **Yujun Cheng:** Data curation, Investigation. **Xu Wang:** Software. **Hui Zhang:** Resources, Supervision.

REFERENCES

- Ajith, K. R., Arunkumar, K., & Hariprasad, C. M. (2015). Effect of dissimilar leading edges on the flow structures around a square cylinder. *Journal of Pressure Vessel Technology*, 137(6). <https://doi.org/10.1115/1.4029656>
- Bi, J., Yu, H., & Ren, H. (2012). Two dimensional numerical simulation of flow over a static square cylinder and a static circular cylinder. *Journal of China Three Gorges University (Natural Sciences)*, 34(1), 41-45. <https://doi.org/10.3969/j.issn.1672-948X.2012.01.010>
- Cakir, E., Akinturk, A., & Allievi, A. (2015, May). A numerical study of fluid structure interaction of a flexible submerged cylinder mounted on an experimental rig. *International Conference on Offshore Mechanics and Arctic Engineering, American Society of Mechanical Engineers*. <https://doi.org/10.1115/OMAE2015-42219>
- Cheng, Y., Duan, D., Liu, X., Yang, X., Zhang, H., & Han, Q. (2022). Numerical study on hydrodynamic performance of underwater manipulator in the subcritical region. *Ocean Engineering*, 262, 112214. <https://doi.org/10.1016/j.oceaneng.2022.112214>
- Chen, H. L., Dai, S. S., Li, J., & Yao, X. L. (2009). Three-dimensional numerical simulation of the flow past a circular cylinder based on LES method. *Journal of Marine Science and Application*, 2(8), 110-116. <https://doi.org/10.1007/s11804-009-8110-4>
- Chen, J. M., & Liu, C. H. (1999). Vortex shedding and surface pressures on a square cylinder at incidence to a uniform air stream. *International Journal of Heat and Fluid Flow*, 20(6), 592-597. [https://doi.org/10.1016/S0142-727X\(99\)00047-8](https://doi.org/10.1016/S0142-727X(99)00047-8)
- Chae, J., Yeu, T., Lee, Y., Lee, Y., & Yoon, S. M. (2020). Trajectory tracking performance analysis of underwater manipulator for autonomous manipulation. *Journal of Ocean Engineering and Technology*, 34(3), 180-193. <https://doi.org/10.26748/KSOE.2019.092>
- Du, Q., Mao, H. Y., & Li, Y. J. (2017) Hydrodynamic characteristics and numerical simulation of flow around square cylinders at different filleting radii. *Marine Sciences*. 41(07), 137-142. <https://doi.org/10.11759/hyhx20161120001>
- Fan, S. B., Lian, L., & Ren, P. (2012). Research on hydrodynamics model test for deepsea open-framed remotely operated vehicle. *China Ocean Engineering*, 26(2), 329-339. <https://doi.org/10.1007/s13344-012-0025-1>
- Fu, M. Y., Wang, S. S., & Wang, Y. H. (2019). Multi-behavior fusion based potential field method for path planning of unmanned surface vessel. *China Ocean Engineering*, 3(5), 583-592. <https://doi.org/10.1007/s13344-019-0056-y>
- Gao, W., Nelias, D., Liu, Z., & Lyu, Y. (2018). Numerical investigation of flow around one finite circular cylinder with two free ends. *Ocean Engineering*, 156, 373-380. <https://doi.org/10.1016/j.oceaneng.2018.03.020>
- Hölscher, N., & Niemann, H. J. (1996). Turbulence and separation induced pressure fluctuations on a finite circular cylinder—application of a linear unsteady strip theory. *Journal of Wind Engineering and Industrial Aerodynamics*, 65(1-3), 335-346. [https://doi.org/10.1016/S0167-6105\(97\)00051-2](https://doi.org/10.1016/S0167-6105(97)00051-2)
- He, S., & Seddighi, M. (2013). Turbulence in transient channel flow. *Journal of Fluid Mechanics*, 715, 60-102. <https://doi.org/10.1017/jfm.2012.498>
- Irwin, R. P., & Chauvet, C. (2007, June). *Quantifying hydrodynamic coefficients of complex structures*. OCEANS 2007-Europe, IEEE. <https://doi.org/10.1109/OCEANSE.2007.4302443>
- Kolodziejczyk, W. (2015). Preliminary study of hydrodynamic load on an underwater robotic manipulator. *Journal of Automation Mobile Robotics and Intelligent Systems*, 9. https://doi.org/10.14313/JAMRIS_4-2015/28
- Kolodziejczyk, W. (2016). Some considerations on an underwater robotic manipulator subjected to the environmental disturbances caused by water current. *Acta Mechanica et Automatica*, 10(1), 43-49. <https://doi.org/10.1515/ama-2016-0008>
- Kolodziejczyk, W. (2018). The method of determination of transient hydrodynamic coefficients for a single DOF underwater manipulator. *Ocean Engineering*, 153, 122-131. <https://doi.org/10.1016/j.oceaneng.2018.01.090>
- Kharghani, M., & PasandidehFard, M. (2022). Turbulence structures in accelerated flow over a flat plate with non-zero pressure gradient. *Journal of Applied Fluid Mechanics*, 15(2), 311-324. <https://doi.org/10.47176/JAFM.15.02.32337>
- Lyn, D. A., Einav, S., Rodi, W., & Park, J. H. (1995). A laser-Doppler velocimetry study of ensemble-averaged characteristics of the turbulent near wake of a square cylinder. *Journal of Fluid Mechanics*, 304, 285-319. <https://doi.org/10.1017/S0022112095004435>
- Mathur, A., Gorji, S., He, S., Seddighi, M., Vardy, A., O'Donoghue, T., & Pokrajac, D. (2018). Temporal acceleration of a turbulent channel flow. *Journal of Fluid Mechanics*, 835, 471-490. <https://doi.org/10.1017/jfm.2017.753>
- McLain, T. W., & Rock, S. M. (1998). Development and experimental validation of an underwater manipulator hydrodynamic model. *The International Journal of Robotics Research*, 17(7), 748-759. <https://doi.org/10.1177/027836499801700705>
- Norberg, C. (1993). Flow around rectangular cylinders: pressure forces and wake frequencies. *Journal of Wind Engineering and Industrial Aerodynamics*, 49(1-3), 187-196. [472](https://doi.org/10.1016/0167-</p></div><div data-bbox=)

[6105\(93\)90014-F](#)

- PasandidehFard, M., & Naeimirad, M. (2022). Turbulent transient boundary layer over a flat plate. *Ocean Engineering*, 244, 110192.
<https://doi.org/10.1016/j.oceaneng.2021.110192>.
- Qu, S., Liu, S. N., & Ong, M. C. (2021). An evaluation of different RANS turbulence models for simulating breaking waves past a vertical cylinder. *Ocean Engineering*, 234, 109195.
<https://doi.org/10.1016/j.oceaneng.2021.109195>.
- Racine, B., & Paterson, E. (2005, June). *CFD-based method for simulation of marine-vehicle maneuvering*. 35th AIAA Fluid Dynamics Conference and Exhibit.
<https://doi.org/10.2514/6.2005-4904>
- Sollicec, C., & Danbon, F. (1999). Aerodynamic torque acting on a butterfly valve. comparison and choice of a torque coefficient.
<https://doi.org/10.1115/1.2823555>
- Safari, F., Rafeeyan, M., & Danesh, M. (2022). Estimation of hydrodynamic coefficients and simplification of the depth model of an AUV using CFD and sensitivity analysis. *Ocean Engineering*, 263, 112369.
<https://doi.org/10.1016/j.oceaneng.2022.112369>
- Wang, X., Jia, Y. Y., Zheng, Y. F., & Fu, S. F. (2021, September). *Numerical simulation of flow around a quasi-square column with $Re=6.8 \times 10^4$* . Proceedings of the 30th National Conference on structural Eng.
<https://doi.org/10.26914/c.cnkihy.2021.019108>
- Wang, H., Meng, Q., & Wang, L., (2007). Analysis on finger dynamics of dexterous underwater hand based on strip theory. *Robot*, 29(2), 160-166.
<https://doi.org/10.13973/j.cnki.robot.2007.02.012>
- Wan, D. C., Shen, Z. R., & Ma, J. (2010). Numerical simulations of viscous flows around surface ship by level set method. *Journal of Hydrodynamics*, 22(1), 271-277. [https://doi.org/10.1016/S1001-6058\(09\)60206-7](https://doi.org/10.1016/S1001-6058(09)60206-7)
- Xu, G., Shen, X., & Yu, K. (2013). Modeling and hydrodynamic performance for a deep ocean manipulator based on numerical approach. *Journal of Computers*, 8(5), 1192-1199.
<https://doi.org/10.4304/jcp.8.5.1192-1199>
- Zhao, M., Cheng, L., & Zhou, T. (2009). Direct numerical simulation of three-dimensional flow past a yawed circular cylinder of infinite length. *Journal of Fluids and Structures*, 25(5), 831-847.
<https://doi.org/10.1016/j.jfluidstructs.2009.02.004>
- Zhang, M., Liu, X., & Tian, Y. (2019). Modeling analysis and simulation of viscous hydrodynamic model of single-DOF manipulator. *Journal of Marine Science and Engineering*, 7(8), 261.
<https://doi.org/10.3390/jmse7080261>
- Zhang, X. S., Wang, J. H., & Wan, D. C. (2020). Numerical techniques for coupling hydrodynamic problems in ship and ocean engineering. *Journal of Hydrodynamics*, 32, 212-233.
<https://doi.org/10.1007/s42241-020-0021-5>